



Journal of Geophysical Research: Oceans

RESEARCH ARTICLE

10.1002/2016JC012196

Key Points:

- The Beaufort Gyre (BG) was intensifying during 1992–2007 in conjunction with changes in sea ice and the upper ocean
- The BG has stabilized since 2008: leveling of sea surface height, ice/ocean speed, and various measures of thermohaline stratification
- The BG intensification and subsequent stabilization are strongly controlled by atmospheric changes in the Canada Basin

Correspondence to: J.

Zhang, zhang@apl.washington.edu

Citation:

Zhang, J., et al. (2016), The Beaufort Gyre intensification and stabilization: A model-observation synthesis, J. Geophys. Res. Oceans, 121, 7933–7952, doi:10.1002/2016JC012196.

Received 28 JUL 2016 Accepted 28 SEP 2016 Accepted article online 4 OCT 2016 Published online 2 NOV 2016

∨ 2016. The Authors.

This is an open access article under the terms of the Creative Commons Attribution-NonCommercial-NoDerivs License, which permits use and distribution in any medium, provided the original work is properly cited, the use is non-commercial and no modifications or adaptations are made.

The Beaufort Gyre intensification and stabilization: A modelobservation synthesis

Jinlun Zhang¹, Michael Steele¹, Kay Runciman¹, Sarah Dewey¹, James Morison¹, Craig Lee¹, Luc Rainville¹, Sylvia Cole², Richard Krishfield², Mary-Louise Timmermans³, and John Toole²

¹Applied Physics Laboratory, University of Washington, Seattle, Washington, USA, ²Department of Physical Oceanography, Woods Hole Oceanographic Institution, Woods Hole, Massachusetts, USA, ³Department of Geology and Geophysics, Yale University, New Haven, Connecticut, USA

Abstract A model-observation synthesis is conducted to investigate changes in the upper ocean circulation and stratification in the Canada Basin [CB] of the Arctic Ocean. Results show that the Beaufort Gyre [BG] has been generally intensifying during 1992–2015 in conjunction with changes in sea ice and the upper ocean including increasing sea surface height [SSH], sea ice and ocean speed, Ekman transport convergence and downwelling, and freshwater content, decreasing ice thickness and upper ocean salinity, shoaling summer halocline and mixed layer, and deepening winter halocline and mixed layer. Increasing Ekman transport convergence draws more water from surrounding areas into the CB, thus lowering SSH in those areas and raising SSH in the CB. The rate of change in the CB began to decrease in 2008 and the BG circulation appears to be stabilizing, if not relaxing slightly. This is reflected in the general plateauing of SSH, the intensity of the sea ice and ocean circulation, and various measures of the CB thermohaline stratification. The BG intensification and subsequent stabilization appear to have been strongly controlled by atmospheric changes in the CB characterized by generally increasing anticyclonic wind circulation and sea level pressure (SLP) before 2008 and falling wind strength and SLP to below-average levels in some years after 2008. Changes in SLP are highly correlated with changes in ocean surface stress curl and downwelling. Since 2008, the magnitude of the stress curl and downwelling in much of the CB has declined, contributing to BG stabilization. The general leveling-off of sea ice thickness also contributes to the stabilization by limiting melt water input to the CB that increases freshwater content. Temperatures in the Near Surface Temperature Maximum layer trended upward slightly over 1992-2015, which is closely correlated with decreasing sea ice thickness. Upper ocean heat content increased over the study period mainly due to strong temperature increases in the summer Pacific Water layer.

1. Introduction

The Beaufort Sea and the larger Canada Basin (CB) of the Arctic Ocean consist of a narrow continental shelf and a sizable deep basin. The upper ocean in the deep basin is strongly stratified and dominated by the well-known anticyclonic Beaufort Gyre (BG) circulation with converging Ekman transport [e.g., Proshutinsky et al., 2009]. The BG is closely associated with the Arctic atmospheric circulation pattern characterized by the Beaufort high pressure cell interacting with the Icelandic and Aleutian low pressure cells [Walsh et al., 1996; Overland et al., 1999]. While the Atlantic Water penetrating into the Arctic Ocean affects the deeper temperature and salinity structure in the CB [e.g., McLaughlin et al., 2009; Mauritzen et al., 2013], the Pacific Water (PW) dominates the upper ocean properties in the region [Coachman and Barnes, 1961; Steele et al., 2004; Shimada et al., 2006; Timmermans et al., 2014, hereinafter T2014].

The PW, a major source of heat, freshwater, and nutrients to the Arctic Ocean, flows through Bering Strait and crosses the vast Chukchi shelf [Codispoti et al., 2005; Woodgate et al., 2012] mainly in three branches: through Herald Canyon and the Central Channel and along the Alaska coast as the Alaska Coastal Current [Weingartner et al., 2005; Brugler et al., 2014]. These three branches of PW penetrate northward into the Arctic Ocean, facilitating summer sea ice retreat [e.g., Zhang et al., 2008; Steele et al., 2010; Woodgate et al., 2010]. The PW also descends into the halocline of the CB, thus ventilating the upper halocline and enhancing ocean stratification via injection of often warm freshwater [e.g., Aagaard et al., 1981; T2014]. The injection of warm summer PW (SPW) leads to the formation of the summer PW layer (SPWL) in the CB, which is

generally characterized by a temperature maximum often with a salinity of 30–33 psu and at depth 40–120 m [Steele et al., 2004; T2014].

The increased air temperature and the decline of sea ice in the Arctic [Hassol, 2004; Serreze et al., 2007] have had a profound impact on the upper ocean physics of the CB, its thermohaline stratification and circulation. Increasing areas of open water, leads, and first-year ice have allowed increased penetration of solar radiation into the upper ocean [Perovich et al., 2007, 2008], warming the surface waters in the CB [Steele et al., 2008; Toole et al., 2010] and enhancing the summer Near Surface Temperature Maximum (NSTM) [Jackson et al., 2010] generally at 15–40 m depth, referred to here as the NSTM layer (NSTML). In situ and satellite data reveal that much of the CB has experienced warming over the past decade. Some of this summer warming is attributed to local atmospheric heating [Steele et al., 2010], and some to intensifying ocean heat transport from the Pacific Ocean through Bering Strait [Woodgate et al., 2005, 2010, 2012].

The regional upper ocean circulation patterns have also been modified in response to changing winds and sea ice cover [Steele et al., 2004; Shimada et al., 2006; Pisareva et al., 2015]. The BG has intensified, with a stronger anticyclonic circulation and increasing stratification, storage of freshwater and stratification in the CB also increased [Proshutinsky et al., 2009; Yang, 2009; Rabe et al., 2011; McPhee, 2013]. These changes are driven by increased Ekman transport convergence (hereafter Ekman convergence) of anomalously low salinity surface waters largely due to sea ice melt [Yamamoto-Kawai et al., 2009; McLaughlin and Carmack, 2010; Krishfield et al., 2014] and Eurasian runoff [Morison et al., 2012], which is associated with stronger cyclonic circulation in the Eurasian Basin. The BG intensification is also due in part to an increase in surface momentum transfer at the ice-ocean interface [Martin et al., 2014, 2016] as the ice cover is thinner and weaker, and therefore moves faster in response to wind forcing [Rampal et al., 2009; Zhang et al., 2012; Kwok et al., 2013]. In addition, the increasing stratification and freshwater content are linked to atmospheric circulation characterized by stronger wind stress curl over the Beaufort Sea in recent years that intensifies water convergence and raises sea surface height (SSH) in the CB [e.g., Giles et al., 2012; Morison et al., 2012].

While previous observational and numerical studies have shed considerable light on the state and variability of the CB climate and its gyre circulation, many of the processes linking the warming of the Arctic, the changing atmospheric circulation, the decreasing sea ice cover, and the variations in the CB stratification dynamics remain unknown. To enhance our understanding of the interplay among the atmosphere, sea ice, and ocean, there have been several integrated programs of intensive observations and numerical simulations to investigate ice-ocean-atmosphere dynamics in the CB, such as the Office of the Naval Research (ONR) Marginal Ice Zone (MIZ) initiative (http://www.apl.washington.edu/project/project.php?id5miz), as well as sustained observing system efforts including the Beaufort Gyre Exploration Project (BGEP, http://www.whoi.edu/website/beaufortgyre/home) and the Seasonal Ice Zone Reconnaissance Surveys (SIZRS, http://www.onr.navy.mil/reports/FY15/agmoriso.pdf).

This study investigates BG variability and concurrent changes in atmosphere-ice-ocean processes, including their linkages and interactions in the CB. For this purpose, we conduct a model-observation synthesis using a coupled ice-ocean model and a range of satellite and in situ observations to explore the large-scale changes in the upper ocean circulation and thermohaline stratification that have occurred in the CB in conjunction with atmospheric and sea ice changes over the past 2–3 decades. The ice-ocean model is the Marginal Ice Zone Modeling and Assimilation System (MIZMAS) that assimilates daily satellite sea ice and sea surface temperature (SST) data and is validated using a range of observational data. Model validation is discussed in section 3 after a brief model description in section 2. In sections 4 and 5, the validated model is used with observations to explore changes in the state of the CB, focusing on the BG intensification and subsequent stabilization (and related hydrographic changes) in the recent decades. Concluding remarks are given in section 6.

2. Brief Model Description

MIZMAS is adapted from the Pan-arctic Ice/Ocean Modeling and Assimilation System (PIOMAS) [Zhang and Rothrock, 2003]. It is a coupled ice-ocean model that assimilates satellite observations of sea ice concentration, following Lindsay and Zhang [2006], and SST, following Manda et al. [2005] [also see Schweiger et al., 2011; Zhang et al., 2015]. SST assimilation is performed only in the open water areas where satellite observations are available. Detailed information about MIZMAS model components, domain, and grid configuration



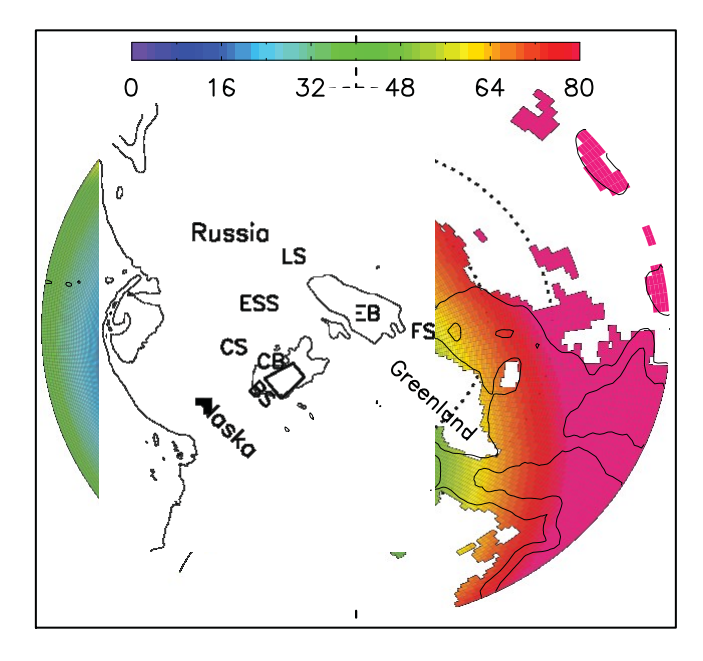


Figure 1. MIZMAS model grid configuration showing the entire model domain covering all ocean areas north of 398N, including the Arctic, North Pacific, and North Atlantic oceans. The colors indicate the model's varying horizontal resolution in km. BS represents the Beaufort Sea, CB the Canada Basin, CS the Chukchi Sea, ESS the East Siberian Sea, LS the Laptev Sea, EB the Eurasian Basin, and FS Fram Strait. The area encircled by thick black lines, bounded by 135-1558W and 74-798N, is referred to as the central Canada Basin (CCB) following Timmermans et al. [2014]. The thin black lines represent isobaths of 500 and 3600 m.

is provided in Schweiger and Zhang [2015], and detailed information about the ice-ocean coupling in the model can be found in Hibler and Bryan [1987] [also see Zhang et al., 1998; Martin et al., 2014]. Here we only give a brief model description.

The sea ice model component of MIZMAS is a thickness and enthalpy distribution (TED) sea ice model [Zhang and Rothrock, 2003; Hibler, 1980]. It has eight categories each for ice thickness, ice enthalpy, and snow depth [Zhang et al., 2010]. The ocean circulation model is based on the Parallel Ocean Program (POP) [Smith et al., 1992]. The POP ocean model was modified by Zhang and Steele [2007] so that open boundary conditions can be specified, and by Zhang et al. [2010] to incorporate tidal forcing arising from the eight primary constituents (M2, S2, N2, K2, K1, O1, P1, and Q1) [Gill, 1982]. The tidal forcing consists of a tide generating potential with corrections due to both the earth tide and self-attraction and

loading, following Marchuk and Kagan [1989]. Vertical ocean mixing is determined based on the K-profile parameterization [Large et al., 1994].

The MIZMAS model domain covers the Northern Hemisphere north of 398N (Figure 1). Its finite-difference grid is based on a generalized orthogonal curvilinear coordinate system with the highest horizontal resolution along the Alaska coast and in the Chukchi, Beaufort, and Bering seas. There are 26 ocean grid cells across Bering Strait providing good resolution of the connection between the Pacific Ocean and the Arctic Ocean. The ocean's vertical dimension has 40 ocean levels of varying thicknesses, with 19 levels in the upper 100 m and the top 16 levels 5 m thick. MIZMAS, a regional model, is one-way nested to a global coupled sea ice-ocean model [Zhang, 2005]. The model was integrated from 1972 to 2015, driven by daily NCEP/NCAR reanalysis surface atmospheric forcing [Kalnay et al., 1996]. Atmospheric forcing and initial conditions are given in Schweiger and Zhang [2015]. Model forcing also includes a monthly climatology of freshwater river runoff in the Arctic Ocean and the Bering Sea [Zhang et al., 2010]. Model results over the period 1992–2015 are used in the model-observation synthesis.

3. Comparison With Hydrographic Observations

In addition to assimilating satellite sea ice concentration and SST, MIZMAS sea ice velocity is calibrated with all available buoy drift data (http://iabp.apl.washington.edu) over the period 1979-2010, with a mean model ice speed bias of about 210% and model-buoy speed correlation of 0.80. Here MIZMAS is further evaluated using ocean salinity and temperature measurements from various platforms. Comparison of simulated temperature and salinity profiles with the observations of the SIZRS Airborne eXpendable CTDs (AXCTDs), which were dropped into open leads from a U.S. Coast Guard aircraft on 20 June and 16 August 2013 at 1508W, 768N, demonstrates how MIZMAS reproduces observed CB temperature profiles within the depth range 40-80 m (Figures 2a and 2d). Whether in June or August, the simulated SPWL temperature maximum and the depth of the maximum are within 0.58C and 5 m of the observations, respectively.

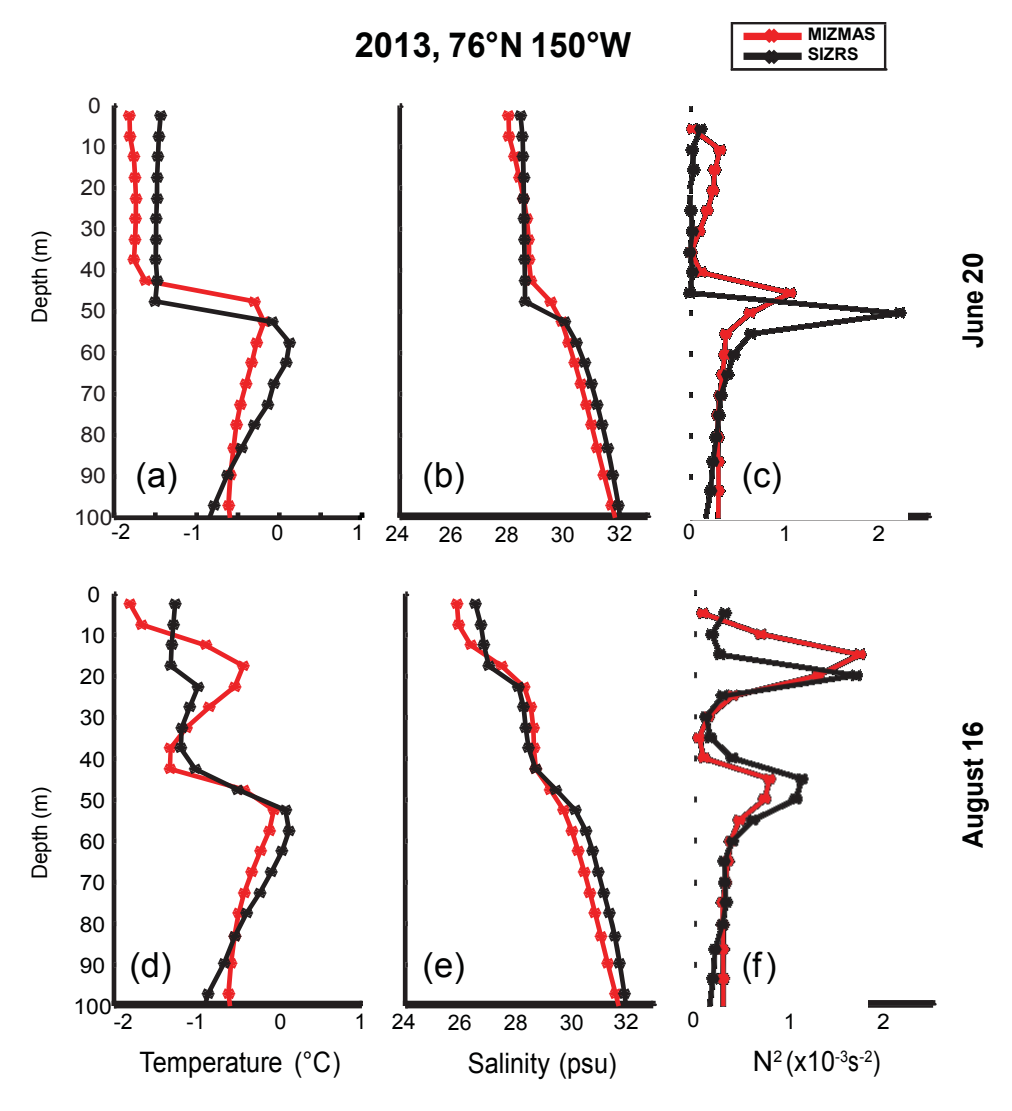


Figure 2. A comparison of MIZMAS simulated (a, d) temperature and (b, e) salinity profiles with SIZRS AXCTD observations on 20 June and 16 August 2013 at 1508W, 768N. The MIZMAS profiles falling within 0.58 latitude and longitude of the SIZRS drop were averaged to create a representative model profile, and the AXCTD profiles were interpolated to the MIZMAS 40-level depth grid before plotting. The plotted dots are located at the centers of the model's vertical ocean levels (the top 16 levels are 5 m thick) in the upper 100 m. Also shown are profiles of buoyancy frequency, N², (c, f) derived with the model output and SIZRS data.

In August 2013, a NSTM was observed and simulated (Figure 2d), but the model overestimates its magnitude, likely due to the NCEP/NCAR reanalysis forcing having a positive bias in shortwave radiation in the Arctic Ocean [Lindsay et al., 2014]. The model simulated temperature of surface waters is cooler than the observations. This bias may be due to the model setting the surface water temperature in a given grid cell at a constant freezing point of 21.88C whenever ice is present in that cell (no SST assimilation performed under ice). This underestimates surface temperatures in CB ice covered areas where surface waters are relatively fresh and the freezing point is often higher than 21.88C.

MIZMAS also reproduces the SIZRS observed salinity profiles in the upper 100 m in 2013 (Figure 2). The mean bias averaged over these two comparisons over the upper 100 m is 0.20 psu. In June, the model captures the observed halocline that was likely formed during the previous winter, with the modeled halocline slightly shallower than the observed (Figures 2b and 2c). During summer, the model replicates the observed surface freshening and therefore the summer halocline as well as the residual winter halocline (Figure 2e) [also see Jackson et al., 2010]. The model underpredicts surface salinity slightly such that the buoyancy frequency, N², peaks at a depth a few meters shallower than the observations (Figure 2f). In particular, both model results and SIZRS observations show that salinity at the depth of the temperature maximum in the

SPWL is mostly between 30.0 and 31.0 psu in 2013, which is consistent with the T2014 analysis of 2013 CTD and Ice-Tethered Profiler (ITP) data in the CB.

MIZMAS is also evaluated with all available salinity and temperature observations from ITPs (http://www.whoi.edu/itp) and autonomous Seagliders in 2014 from the Beaufort Sea and CB (Figures 3–6). There were 11 ITPs (ITP 70, 77–82, and 84–87, with trajectories shown in Figure 4a), deployed by the ONR MIZ field campaign, BGEP, Chinese research vessel Xuelong, and Korean research vessel Araon, and two Seagliders (trajectories in Figure 5a), deployed in support of the ONR MIZ field campaign. ITP observations are distributed throughout the year while Seaglider observations are confined to August and September. Daily averaged T and S profiles are used, which is equivalent to a 6–16 km (ITP) and \$20 km (Seaglider) lateral scale; there is mesoscale and submesoscale variability in these observations not represented in the model.

Comparison with ITP77 (longest trajectory; Figure 4a, pink line) shows that the model tends to overestimate salinity in the upper 40 m and underestimate it at 40–120 m depth (Figures 3a–3c), although the timing and the magnitude of the freshening in the upper 40 m in summer (July–September) is well simulated. The model has a positive salinity bias in late spring (spring is defined as April–June) along this particular ITP trajectory, which contributes to a positive bias (often <0.5 psu) during most of the summer in the upper 40 m. As salinity primarily determines density in cool polar waters, the modeled stratification is slightly too weak near 50 m and slightly too strong near 100 m.

MIZMAS simulated temperature in the surface waters is lower than observations along the ITP77 trajectory (Figures 3d–3f). Both model results and observations show the formation of a NSTM about the same time during summer at 15–40 m depth (see the discussion in Gallaher et al. [2016] based on observations). As summer progresses, the NSTM tends to deepen in the model results and observations (Figures 3d and 3e), likely caused by Ekman convergence and downwelling [Steele et al., 2011]. The simulated NSTM is warmer than observed by ITP77 (Figure 3f). This is again likely linked to the positive bias of the shortwave radiation forcing in the NCEP/NCAR reanalysis. The model reproduces well the temperature profiles in the SPWL (40–80 m) with mostly small biases below 0.58C (Figure 3f).

In addition to ocean salinity and temperature measurements, ITP77 also measured ocean velocity [Cole et al., 2015], which allows us to perform model-observation velocity comparisons. The model simulated current speed profile tracks well with ITP77 observations in about the upper 50 m, with both showing a general acceleration in the upper 50 m along the ITP77 trajectory. Below 50 m, ITP77 measured some strong eddies with large velocities, which MIZMAS is unable to replicate owing to its limited resolution.

Comparisons with all available daily average temperature and salinity observations along the trajectories of the 11 ITPs and two Seagliders show again that the model is biased low in temperature in the upper 15 m (Figures 4 and 5). This is also reflected in 10 day-averaged ITP temperatures in the upper 15 m and the differences between 10 day model averages and the ITP estimates (Figures 6a and 6b). Although the model tends to overestimate the magnitude of the NSTM measured by an AXCTD in 2013 or by ITP77 in 2014 (Figures 2 and 3), when compared to all ITP and Seaglider temperature data in the depth range 15–40 m, the model has small mean biases, 20.19%C against ITPs and 0.06%C against Seagliders (Figures 4b and 5b). This is because the NSTM is limited in space and time, and is why the differences between 10 day average model and ITP temperatures are small in much of the Beaufort Sea (Figures 6c and 6d). The model also calculates the temperature of the SPWL (40–80 m) with near zero mean bias (Figures 4b and 5b), but overestimates the SPWL temperatures north of 80%N in the CB (Figures 6e and 6f). Overall, when all the model and observation data points over the whole upper 150 m are compared, the model exhibits small mean temperature biases of 0.08%C (against ITPs) and 0.05%C (against Seagliders) and high correlations of 0.72 and 0.80 (Figures 4 and 5).

Like the comparison with ITP77 (Figure 3), the model overestimates salinity in the upper 40 m, while underestimating it below 40 m depth, when compared to all available ITP and Seaglider salinity data (Figures 4c and 5c). The simulated salinity is closely correlated with ITP observations in all four depth ranges, with correlations ranging from 0.59 to 0.82 (Figure 4c). Meanwhile, apart from the upper 15 m, the simulated salinity is highly correlated with the Seaglider observations in three depth ranges below 15 m, with correlations ranging from 0.86 to 0.94 (Figure 5c). Overall, for the whole upper 150 m, the model has low mean salinity biases of 20.01 psu (against ITPs) and 20.10 psu (against Seagliders) and high correlations of 0.93 and 0.98 (Figures 4c and 5c).

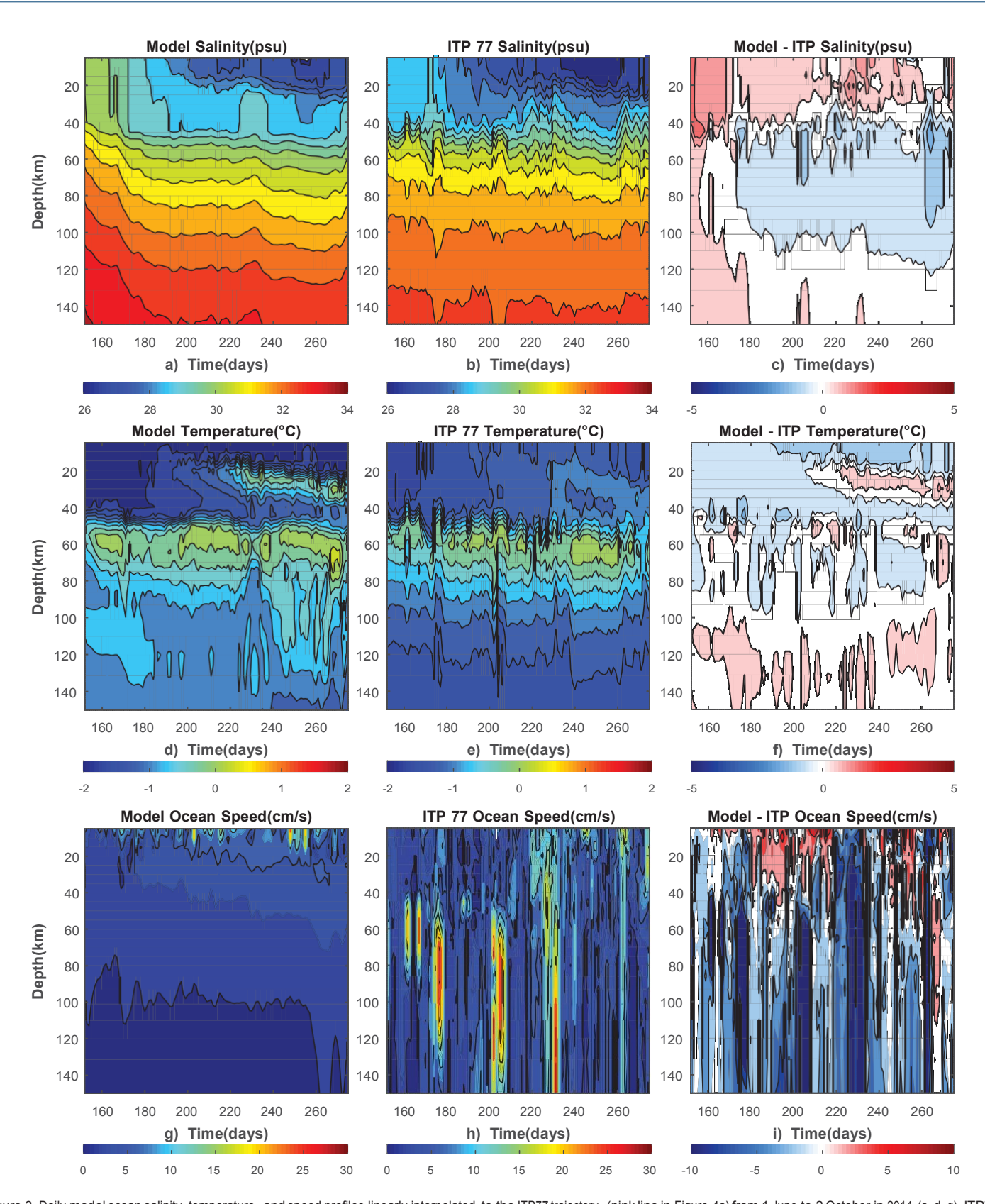


Figure 3. Daily model ocean salinity, temperature, and speed profiles linearly interpolated to the ITP77 trajectory (pink line in Figure 4a) from 1 June to 2 October in 2014 (a, d, g), ITP77 daily averaged salinity, temperature, and speed linearly interpolated to the model depth (b, e, h), and difference in salinity, temperature, and speed between the model and ITP77 along the trajectory (c, f, i). Contour intervals are 0.5 psu for salinity, 0.25%C for temperature, 2 cm s²¹ for speed, and 0.5 psu, 0.5%C, and 2 cm s²¹ for salinity, temperature, and speed differences.

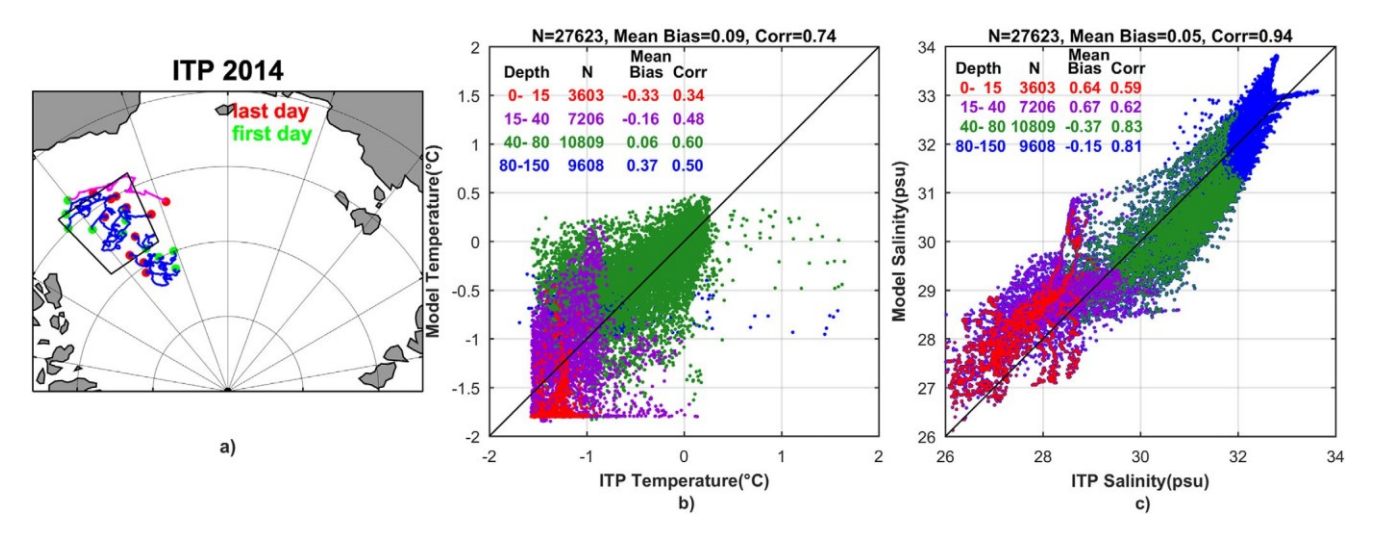


Figure 4. Comparisons with all available daily ITP temperature and salinity data in 2014. (a) Tracks of available 11 ITPs (ITP70, ITP77–82, and ITP84–87) in the Beaufort Sea during 1 June to 31 December 2014. The pink line in Figure 4a is the track of ITP77 along which both model results and ITP observations are displayed in Figure 3. (b) and (c) Temperature and salinity comparisons over various depth ranges (0–15 m, 15–40 m, 40–80 m, and 80–150 m). The number of observations and corresponding model results (N), mean model bias, and model-observation correlation (Corr) for each depth range are indicated. The total number of observations and overall mean bias and correlation are shown at the top of Figures 4b and 4c. The box in Figure 4a represents the central Canada Basin (CCB, also see Figure 1).

In addition to the above comparisons, SIZRS observations of salinity profile variability from 2012 to 2014 are examined and qualitatively compared with MIZMAS results. MIZMAS simulated depths of isohalines 31 and 33 are compared with those derived by T2014 using CTD data over the period 2003–2013. In particular, MIZMAS simulated salinity at the depth of the SPWL temperature maximum in 2007 and 2013 agrees well with the T2014 analysis from these 2 years. These comparisons are described in sections 4 and 5.

4. The Beaufort Gyre Intensification

The simulated BG manifests as relatively high SSH in the CB (Figures 7a and 7b). The BG intensification in recent decades is illustrated by a comparison between the 2004–2015 mean SSH and the 1992–2003 mean (Figure 7c). The simulated mean SSH in the later period is • 20 cm higher in the central CB than in the earlier period. In surrounding seas, however, the simulated SSH in the later period is lower, including the

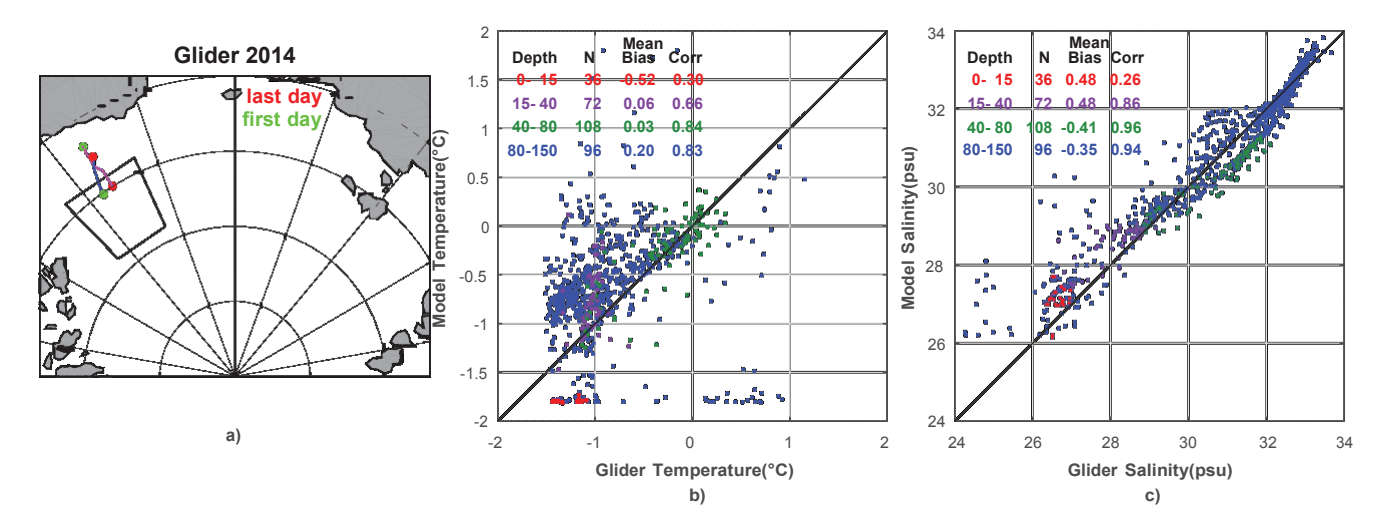


Figure 5. Comparisons with all available daily Seaglider temperature and salinity data in 2014. (a) Tracks of the two Seagliders in the Beaufort Sea over the periods 11–31 August and 15–30 September 2014. (b) and (c) Temperature and salinity comparisons over various depth ranges (0–15 m; 15–40 m, 40–80 m, and 80–150 m). The number of observations and corresponding model results (N), mean model bias, and model—observation correlation (Corr) for each depth range are indicated. The total number of observations and overall mean bias and correlation are shown at the top of Figures 5b and 5c.

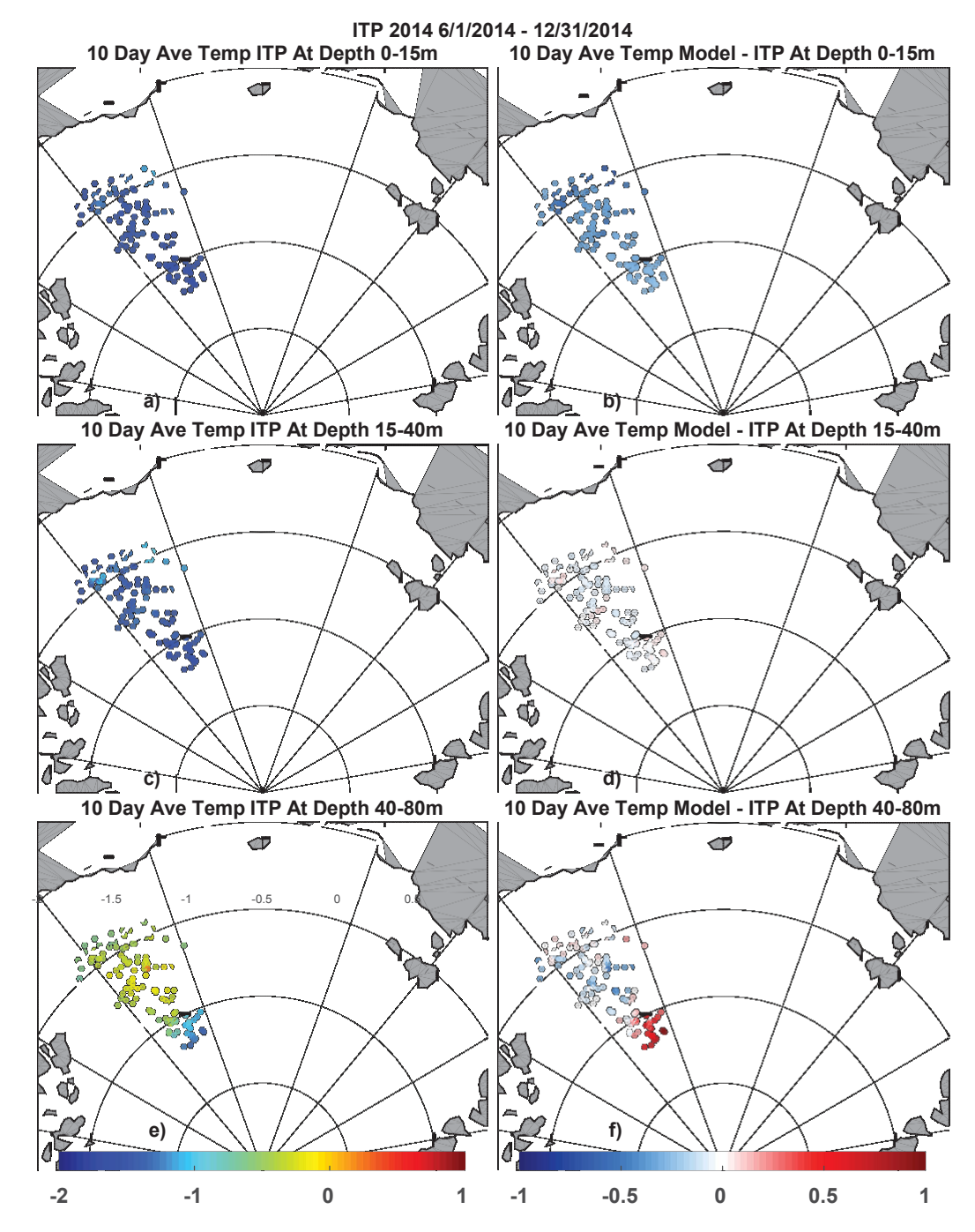


Figure 6. (a, c, e) Observed 10 day mean temperature (8C) averaged over various depth ranges (0–15 m, 15–40 m, 40–80 m) for the 11 ITPs in the Beaufort Sea during 1 June to 31 December 2014. (b, d, f) Model bias of the 10 day averages (model minus observation) over the depth ranges

Beaufort Sea shelf region, most of the Chukchi, East Siberian, and Laptev seas, and part of the Eurasian Basin. Enhanced Ekman convergence in the later period draws surface waters from those surrounding areas toward the CB as the BG intensifies. The BG intensification is further illustrated by the upward trend in the SSH averaged in the central Canada Basin (CCB, defined by T2014; also see Figure 1) over the period 1992–2015 (Figure 8a).

The BG intensification is linked to changes in atmospheric circulation, characterized in the Arctic Ocean by the Beaufort high pressure cell and the Icelandic low pressure cell with an anticyclonic surface wind

AGU. Journal of Geophysical Research: Oceans

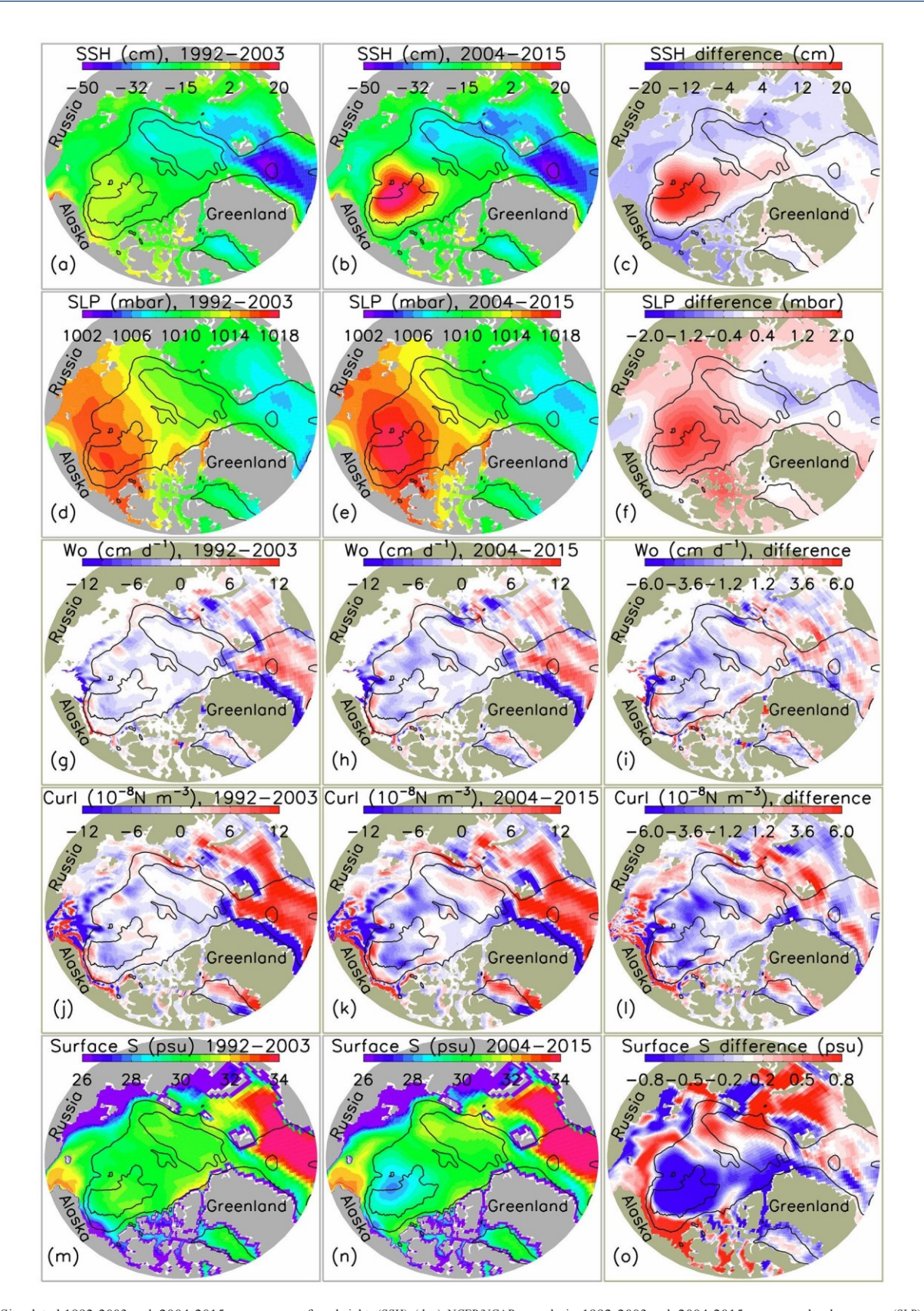


Figure 7.(a, b) Simulated 1992-2003 and 2004-2015 mean sea surface height (SSH), (d, e) NCEP/NCAR reanalysis 1992-2003 and 2004-2015 mean sea level pressure (SLP), (g, h) simulated ocean vertical velocity (W_o , upward positive) at 60 m, \hat{G} , k) curl of ocean surface stress (curl (T) =V' XT), and (m, n) surface salinity (5), and the differences between the 2004-2015 mean and the 1992-2003 mean (2004-2015 mean minus 1992-2003 mean) of these variables (c, f, i, l, and o). The black lines represent isobaths of 500 and 3600 m.

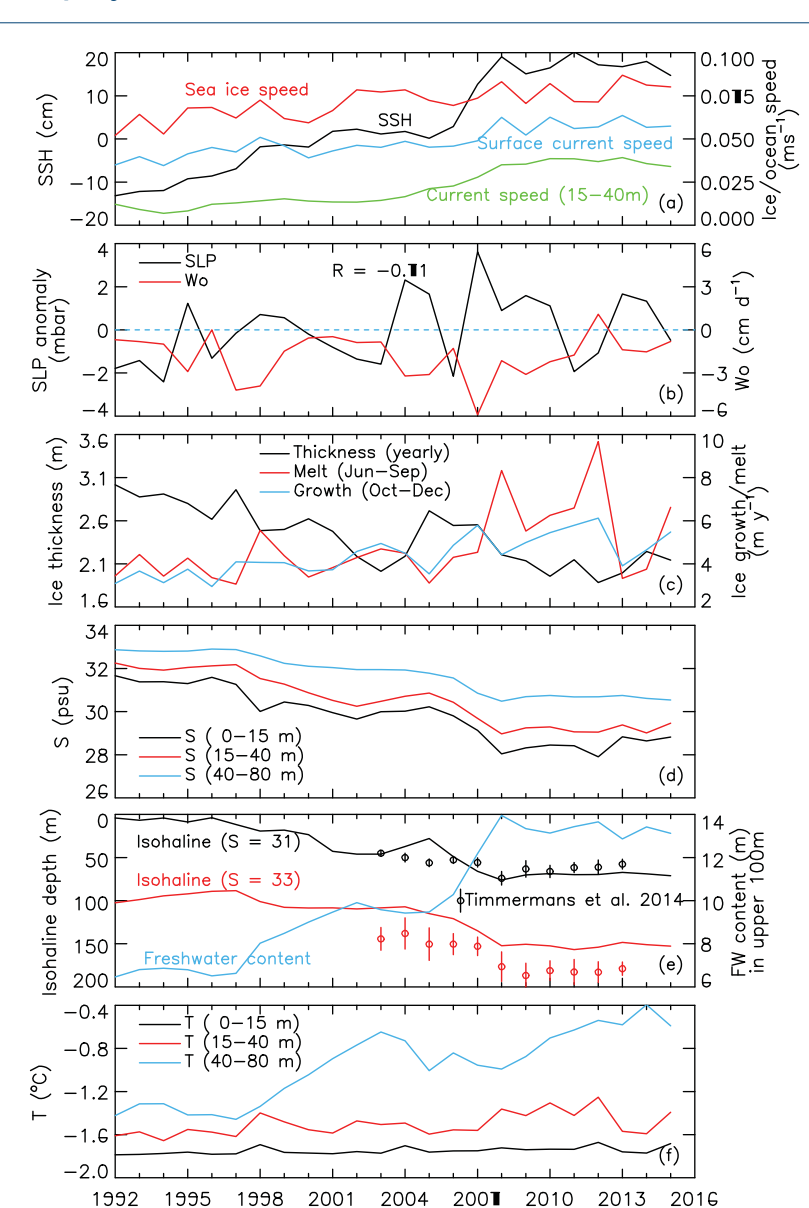


Figure 8. Averages over the central Canada Basin (CCB, defined as the area within 135–150°W, 74–79°N; see Figure 1) of (a) simulated annual mean SSH, sea ice speed, and current speed at the surface and in the depth range 15–40 m, (b) NCEP/NCAR reanalysis annual mean SLP anomaly from the 1992–2015 mean and simulated annual mean ocean vertical velocity (W_o) at 60 m, (c) simulated annual mean sea ice thickness, June–September mean ice melt rates, and October–December mean ice growth rates, and (d) simulated annual mean ocean salinity (S) at different depth ranges, (e) the depths of isohalines with \$531 and \$533 and freshwater (FW) content in the upper 100 m of the ocean, and (f) ocean temperature (T) at different depths. Correlation between SLP anomaly and W_o at 60 m is listed in Figure 8b. In Figure 8e, annual mean CTD observations and error bars of the isohaline depths taken in the CCB are from Timmermans et al. [2014].

circulation in the CB (Figure 9a), and reflected in the NCEP/NCAR reanalysis sea level pressure (SLP) (Figures 7d and 7e) [see Walsh et al., 1996]. The reanalysis SLP in the CB is considerably higher in 2004–2015 than in 1992–2003 (Figure 7f), indicating that the Beaufort high pressure cell was stronger in the later period. This is also reflected in the time series of annual mean SLP anomaly averaged over the CCB (Figure 8b). The annual mean SLP anomaly shows considerable interannual fluctuations between 1992 and 2015. However, there were more years with relatively high mean SLP in the later period than in the earlier period. Particularly high SLP occurred in 2004, 2005, and 2007 with the latter year having the highest mean SLP over the period 1992–2015. During or after these high SLP years, the simulated SSH in the CCB increases rapidly (Figure 8a). The more frequent occurrence of relatively high SLP in 2004–2015 led to a stronger anticyclonic wind circulation in the CB, which is illustrated by the anticyclonic wind velocity difference field between the 2004–2015 mean and the 1992–2003 mean (Figure 9b).

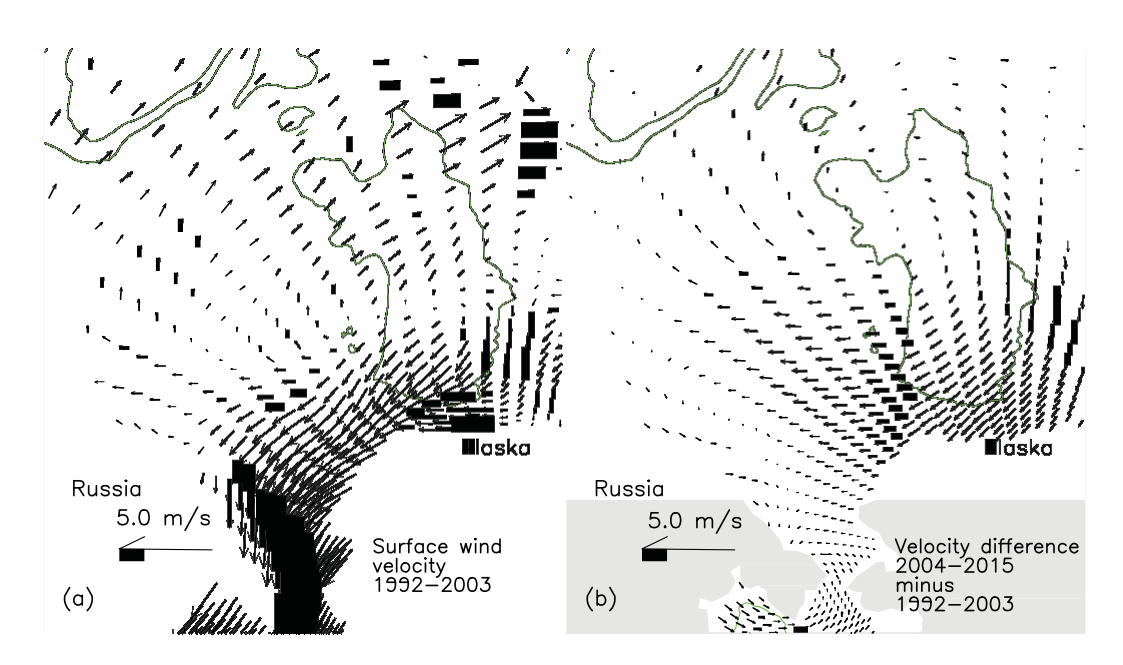


Figure 9. (a) NCEP/NCAR reanalysis 1992-2003 mean surface (at 10 m) wind velocity and (b) the difference between the 2004-2015 mean and the 1992-2003 mean. The wind velocity vectors are plotted on the model grid with every 36th velocity vector drawn. The green lines represent isobaths of 65, 500, 2200, and 3600 m.

The BG intensification is also reflected in changes in ocean currents in the CB. The simulated pattern of ocean currents includes an anticyclonic circulation in the upper ocean of the CB, while in the Chukchi Sea the PW moves northward in three pathways: Herald Canyon, the Central Channel, and Alaska coast (Figure 10a). The simulated anticyclonic circulation in the CB is stronger in 2004-2015 than in 1992-2003 because of greater momentum transfer at the ocean surface in response to the intensified Beaufort high pressure cell and anticyclonic wind circulation. As a result, the ocean horizontal velocity difference between these two periods displays a strong anticyclonic circulation pattern in the CB (Figure 10b), with increased current speed as well as sea ice motion in the later period (Figure 8a; also see Yang [2009]; McPhee [2013]; Morison et al. [2012]).

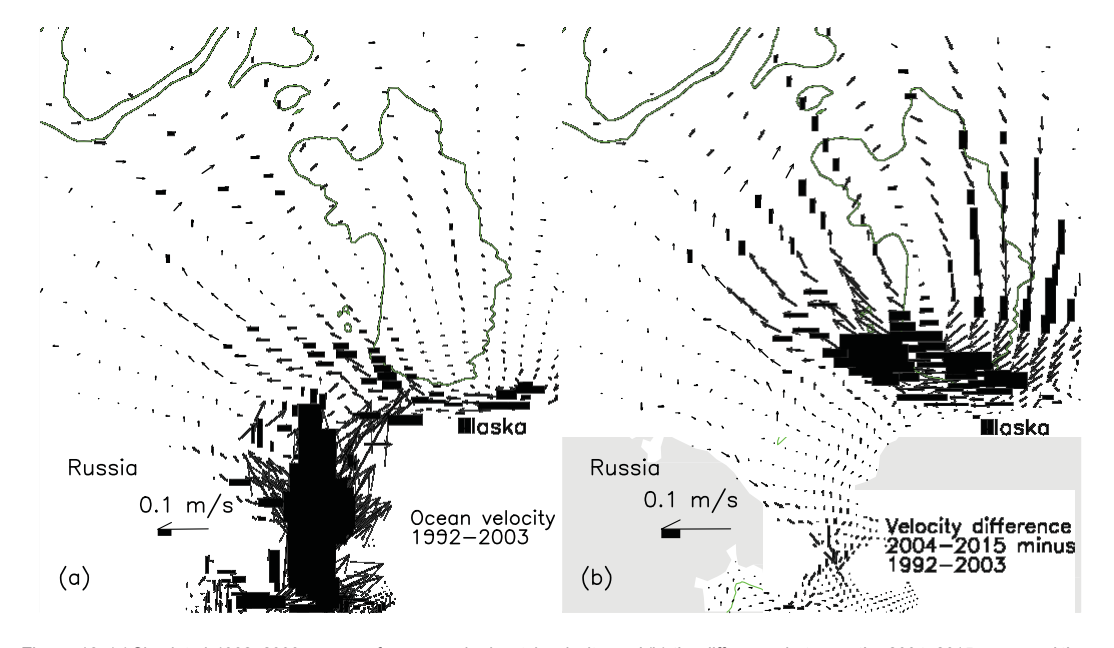


Figure 10. (a) Simulated 1992-2003 mean surface ocean horizontal velocity and (b) the difference between the 2004-2015 mean and the 1992-2003 mean. Every 36th velocity vector is drawn. The green lines represent isobaths of 65, 500, 2200, and 3600 m.

The increased sea ice mobility in recent years is also linked to changes in sea ice properties. Ice thickness generally decreases over the period 1992–2015 because of increasing ice melt in late spring and summer (Figure 8c), in response to Arctic warming and increasing surface solar heating [Hassol, 2004; Serreze et al., 2007; Perovich et al., 2007, 2008]. A thinner ice cover is more responsive to wind forcing and moves faster [Rampal et al., 2009; Zhang et al., 2012; Kwok et al., 2013]. Thus wind forcing is communicated more directly to the ocean across the air-ice-ocean boundary layer [Martin et al., 2014], which also contributes to the BG intensification as reflected in the increasing strength of surface ocean currents (in the first ocean level centered at 2.5 m) and currents at 15–40 m depth (Figures 8a and 10b).

The increasing anticyclonic BG circulation influences the intensity of Ekman transport and hence the strength of upwelling and downwelling in the CB, as reflected in MIZMAS ocean vertical velocity. The simulated ocean vertical velocities (W_o) at 60 m (and at other depths, not shown) are characterized by negative values (downwelling) throughout most of the CB and positive values (upwelling) at the Beaufort Sea shelf break (Figures 7g and 7h). As the BG intensifies during 2004–2015, downwelling is enhanced in the CB (Figure 7i) because of stronger converging Ekman transport, which is illustrated by more negative values in the simulated curl of the stress (curl (s) $5\,\text{r-}3s$) at the ocean surface (Figures 7j–7l). Enhanced downwelling in the CB coincides with enhanced upwelling at the Beaufort Sea shelf break (Figure 7i). As expected, the simulated vertical velocity at 60 m and the simulated curl of the stress at the ocean surface are highly correlated in space and time (Figures 7j–7l; also see Yang [2009]). The correlation between the annual means of these two variables averaged over the CCB is R $5\,0.98$ over the period 1992–2015. The correlation between the simulated curl of the stress at the ocean surface and SLP in the CCB is R $5\,20.75$. Correspondingly, the vertical Ekman velocity is (negatively) correlated (R $5\,20.71$) with the reanalysis SLP in the CCB (Figure 8b). Higher SLP in the CB is associated with stronger Ekman transport convergence.

The BG intensification with enhanced downwelling in the CB and upwelling at the Beaufort Sea shelf break leads to changes in the upper ocean salinity. Compared to the period 1992–2003, the simulated ocean surface salinity during 2004–2015 decreases markedly in the CB, in part because of the enhanced convergence of relatively fresh surface waters (Figures 7m–7o). Meanwhile, ocean surface salinity increases in the Beaufort Sea shelf break region (Figure 7o) because of enhanced upwelling there. Surface salinity also increases in much of the Chukchi and East Siberian shelf and shelf break regions. This latter change is due to horizontal advection associated with anticyclonic BG circulation, which tends to transport upwelled, relatively salty water from the Beaufort Sea shelf break region to the Chukchi and East Siberian shelves (not shown).

The simulated CB salinity down to 80 m also decreases between 1992 and 2015 (Figure 8d), partly due to enhanced Ekman convergence. This is illustrated by the high correlation (R 5 20.98) between the simulated ocean salinity in the upper 15 m (Figure 8d) and SSH (Figure 8a) in the CCB. The decreases in upper ocean salinity are also linked to increases in ice melt and decreases in ice thickness (Figure 8c). The variability in upper 15 m salinity in the CCB is closely correlated with that of the June–September mean ice melt (R 5 20.70) and that of annual mean ice thickness (R 5 0.85) (see also Krishfield et al. [2014]).

As salinity generally decreases in the upper 80 m in the CB over the period 1992–2015, the simulated depths of the \$531 and \$533 isohalines and the freshwater content in the upper 100 m generally increase (Figure 8e). Apart from 2005, the simulated \$531 isohaline depth is in good agreement with that obtained by T2014 using CTD observations from the period 2003–2013. The model has a mean bias of about 30 m in underestimating the \$533 isohaline depth when compared to the CTD derived data of T2014 (Figure 8e), but MIZMAS captures well the interannual variability of the CTD-derived \$533 isohaline depth over the period 2003–2013 (Figure 8e). For example, the model predicts an increase in the isohaline depth from 2007 to 2008 that is similar in amplitude to the CTD observations.

The decreases in ocean salinity in recent years are also reflected in vertical salinity profiles. The simulated seasonal evolution (from June to January) of salinity profiles averaged in the CCB over the period 1992–2015 shows summer freshening in the upper ocean, confined mainly to the upper 40 m (Figure 11a) and strongly influenced by ice melting (Figure 8c). The upper ocean salinity starts to decrease in June and reaches its lowest levels in August and September when the NSTM is the warmest (Figure 11b). From October onward, the upper ocean salinity increases again because of ice growth and mixing with deeper waters (Figure 11). Over the period 1992–2015, the simulated upper ocean salinity decreases (Figures 12a, 12c, and

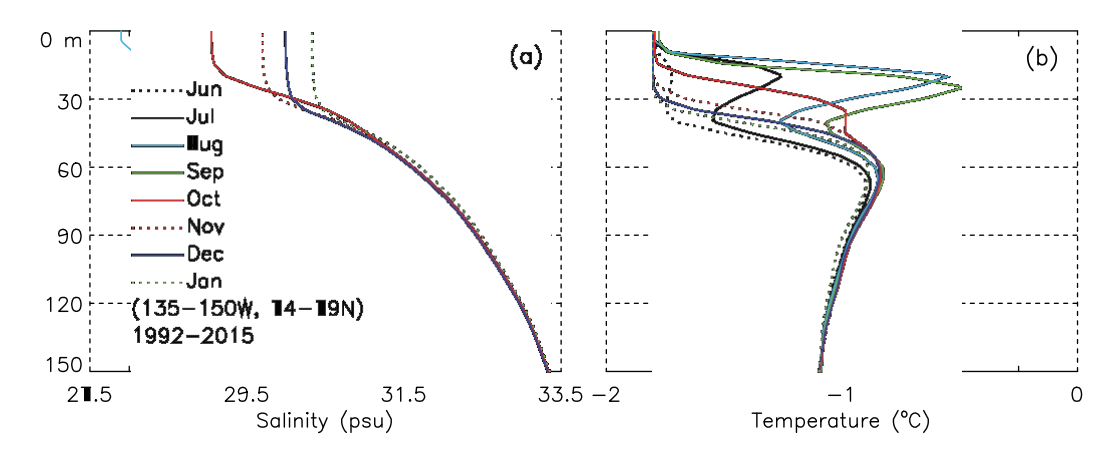


Figure 11. Simulated 1992–2015 mean monthly evolution (from June to January) of ocean salinity 870 and temperature profiles averaged over the CCB.

12e), while the upper ocean temperature maximum layers (both the NSTML and the SPWL) tend to warm (Figures 12b, 12d, and 12f). For example, MIZMAS shows that the salinity at the depth of the SPWL temperature maximum is largely between 30.5 and 32.0 psu in 2007, which is greater than the corresponding 30.0-

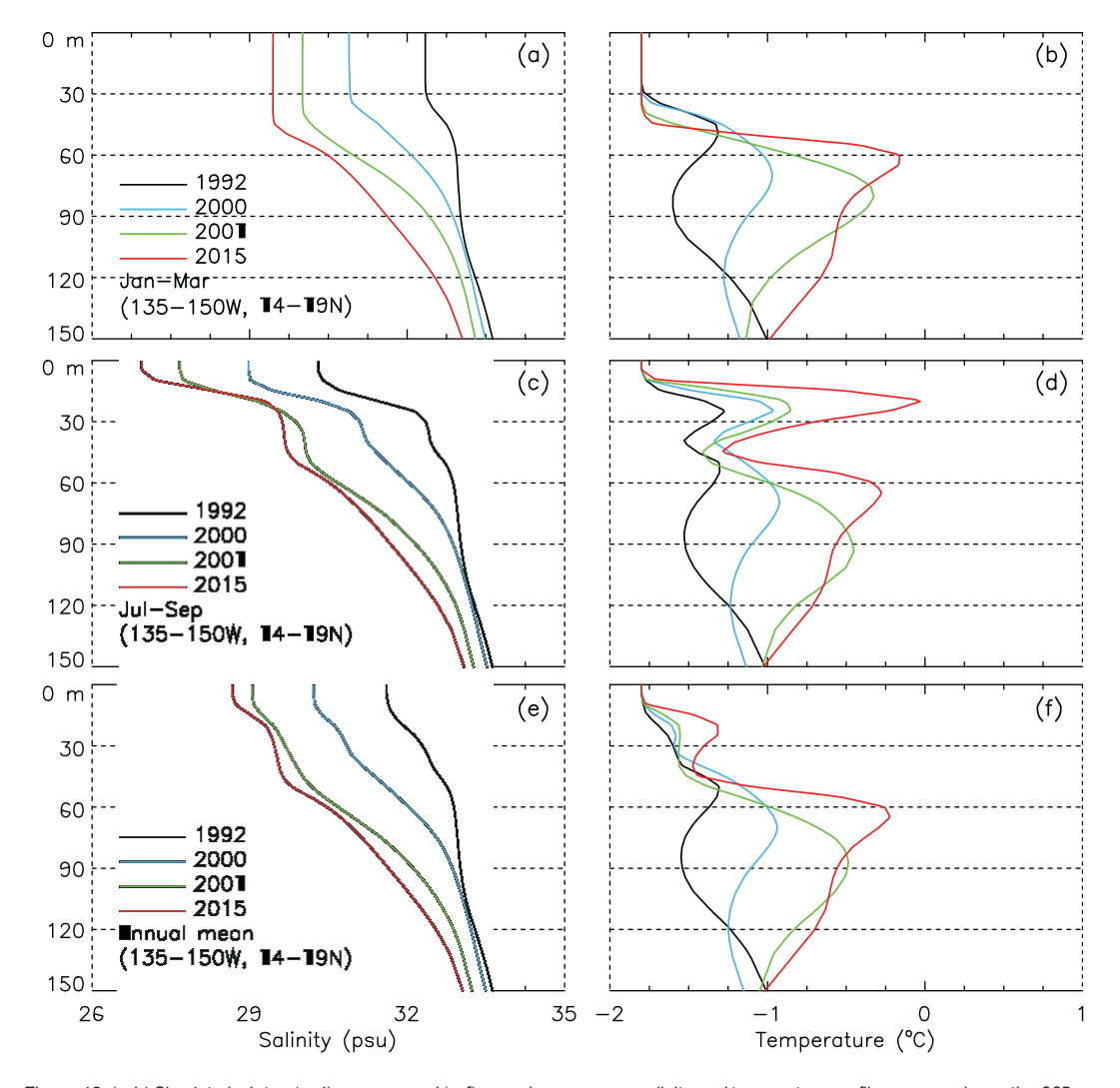


Figure 12. (a, b) Simulated winter, (c, d) summer, and (e, f) annual mean ocean salinity and temperature profiles averaged over the CCB for 2009, 2011, 2013, and 2015.

31.0 psu values derived for 2013 (Figures 2c and 2d). These values for both 2007 and 2013 are all in good agreement with T2014 analysis of CTD and ITP data from these 2 years.

Freshening during summer contributes to the shoaling of the ocean mixed layer over the period 1992—2015, as both the halocline and thermocline become shallower (Figures 12c and 12d). The simulated summer shoaling of the ocean mixed layer was also observed by Peralta-Ferriz and Woodgate [2015] using available summer ship-based hydrographic observations from 1979 to 2012. During winter, the model shows increasing mixed layer depth over the period 1992–2015 as both the halocline and thermocline deepen (Figures 12a and 12b), consistent with observations of CB halocline and nutricline deepening over the period 2003–2009 [McLaughlin and Carmack, 2010]. This is in part because of the generally stronger Ekman downwelling in the CB during 2004–2015 (Figures 7i, 7l, and 8b), which tends to push the pycnocline deeper [e.g., McLaughlin and Carmack, 2010; Yang, 2009]. Deeper winter mixed layers are also a consequence of the stronger surface stress associated with stronger ice motion and hence momentum transfer at the ice-ocean interface (Figures 8a and 10b) [e.g., Rampal et al., 2009; Martin et al., 2014], which enhances ocean mixing. The shoaling of the summer halocline and deepening of the winter halocline over 1992–2015 are illustrated in the annual mean salinity profiles (Figure 12e).

5. The Beaufort Gyre Stabilization

While the BG has been generally intensifying over the past 2–3 decades, it appears to have stabilized during 2008–2015. This is illustrated in the simulation by a plateauing of SSH, the strengths of the ocean currents and ice motion (Figure 8a), freshwater content, the depths of the 31 and 33 isohalines (Figure 8e), and overall upper-ocean salinity (Figure 8d) over the period. In fact, the simulated salinity in the upper 15 m increases slightly (Figure 8d). This tendency is consistent with the SIZRS observations that the June–August salinity in the upper 15 m increased by §2 psu from 2012 to 2014 along 1508W within the CCB. The BG stabilization is also illustrated by the flattening of the observed 31 and 33 isohaline depths calculated by T2014 over the period 2008–2013 (Figure 8e; also see Figure 9 in T2014). In particular, the observations indicate a slight decrease in the \$5 31 isohaline depth during 2008–2013 (Figure 8e; Figure 9 in T2014), indicating that the upper ocean freshening in the CB, associated with the BG intensification, stopped, or reversed slightly.

The BG stabilization is also reflected in the simulated salinity profiles in recent years (Figure 12). The model shows relatively small salinity changes in the upper 150 m of the CCB averaged over the years of 2009, 2011, 2013, and 2015 when compared to earlier years (Figured 13a, 13c, and 13e). In particular, the model shows that the upper ocean in the CCB is saltier in 2013 than in 2009. This is consistent with the CTD and ITP observations that the isohaline depth of \$ \(\frac{5}{2} \) 31 is shallower in 2013 than in 2009 (Figure 8e; T2014). The model also shows that the upper ocean is saltier in 2015 than in 2013. These are additional signs of the BG stabilizing, if not relaxing slightly. However, over the stabilization period 2009–2015, temperature profiles continue to vary considerably within the NSTML in summer and the SPWL all year (Figures 13b, 13d, and 13f).

Like the BG intensification, the BG stabilization may be explained by changes in the atmospheric circulation that influence SLP variability. After 2007, which has the maximum CCB SLP over the period 1992–2015, SLP relaxed to a moderately high level (2008–2010, 2013–2014) or a below-average level (2011–2012, 2015) (Figure 8b). SLP was, in fact, slightly lower throughout much of the CB in 2012–2015 than in 2008–2011 (Figures 14d–14f). This is why the simulated SSH does not continue to rise during 2008–2015 (Figure 8a). Instead, it decreases slightly during 2012–2015 in much of the CB (Figures 14a–14c), in response to the changes in wind forcing as manifested by SLP.

As SLP and SSH are decreasing slightly from the period 2008–2011 to the period 2012–2015, Ekman convergence is reduced. As a result, both downwelling in much of the CB and upwelling in much of the Beaufort Sea shelf break region are lower in 2012–2015 than in 2008–2011 (Figures 14g–14i), corresponding closely to changes in the ocean surface stress curl (Figures 14j–14l). This leads to lower surface salinity on the Beaufort Sea shelf and in the shelf break region and slightly higher surface salinity in much of the CB (Figures 14m–14o). The slightly higher surface salinity in the CB during 2012–2015 is consistent with the simulated salinity profiles in recent years (Figures 13a, 13c, and 13e). Changes in surface salinity during 2012–2015, relative to 2008–2011, are simulated for other regions of the Arctic Ocean as well, such as the East Siberian

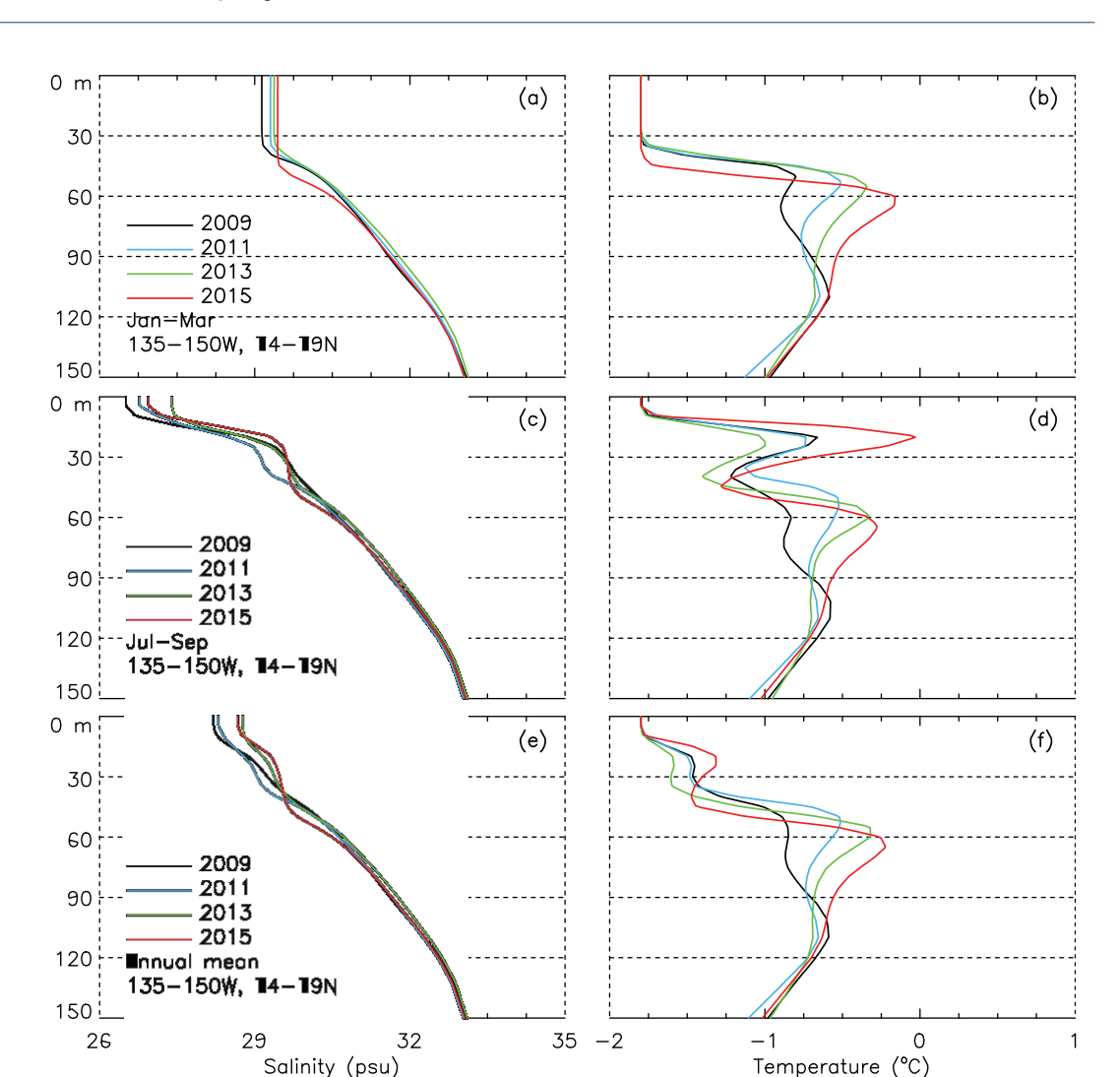


Figure 13. (a, b) Simulated 2008–2011 and 2012–2015 mean sea surface height (SSH), (d, e) NCEP/NCAR reanalysis 2008–2011 and 2012–2015 mean sea level pressure (SLP), (g, h) simulated ocean vertical velocity (W_o) at 60 m, (j, k) curl of the stress at the ocean surface, and (m, n) surface salinity (S), and the differences between the 2012–2015 mean and the 2008–2011 mean (2012–2015 mean minus 2008–2011 mean) of these variables (c. f. i, l, and o).

and Laptev seas and the Eurasian Basin (Figures 14m–14o). These changes are likely also linked to changes in atmospheric circulation reflected in the changes in SLP (Figure 14f).

Sea ice conditions during 2008–2015 may have also contributed to the BG stabilization. Unlike many of the previous years, the simulated ice thickness averaged over the CCB remains nearly constant during 2008–2015 (Figure 8c). In fact, ice thickness in the CCB rebounds to some extent in 2013–2014 after reaching the 2012 minimum when Arctic summer sea ice extent reached its record low of the satellite era (since 1978) [Parkinson and Comiso, 2013; Zhang et al., 2013]. According to MIZMAS, the lowest average ice thickness in 2012 is the product of the highest June–September ice melt in the simulation period, while the ice thickness rebound in the following 2 years is linked to a precipitous drop in summer ice melt (Figure 8c). Thus the moderation of sea ice melt may have contributed to BG stabilization in recent years.

While the simulated BG and the upper ocean freshwater content stabilize in 2008–2015, the simulated heat content in the upper 150 m in the CCB continues to increase (Figure 8f). Note that MIZMAS shows little interannual temperature variability in the upper 15 m of the CCB whether in 2008–2015 or over the period 1992–2015 (Figure 8f) because the area is mostly covered by sea ice and therefore the simulated surface waters are often at the specified freezing point. There is a small positive temperature trend in the simulated NSTML (15–40 m) over the period 1992–2015 when the simulated sea ice thickness is generally decreasing.

AGU. Journal of Geophysical Research: Oceans

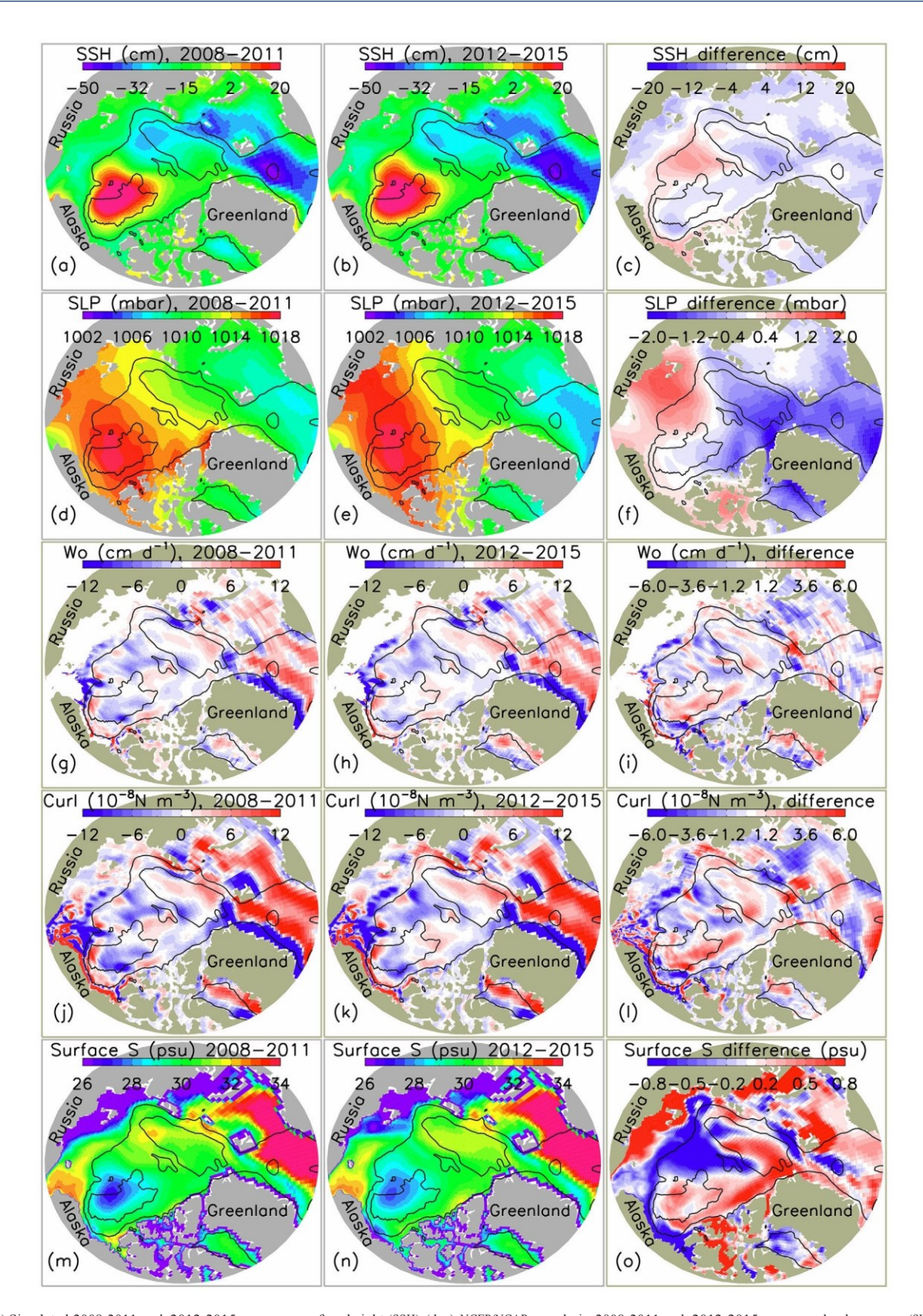


Figure 14. (a, b) Simulated 2008-2011 and 2012-2015 mean sea surface height (SSH), (d, e) NCEP/NCAR reanalysis 2008-2011 and 2012-2015 mean sea level pressure (SLP), (g, h) simulated ocean vertical velocity (W_{0}) at 60 m, \hat{G} , k) curl of the stress at the ocean surface, and (m, n) surface salinity (5), and the differences between the 2012-2015 mean and the 2008-2011 mean (2012-2015 mean minus 2008-2011 mean) of these variables (c, f, i, I, and o).

The correlation between ice thickness and NSTML temperature in the model is quite high at R 5 20.75. During 2008–2015 with a stabilizing BG, the simulated temperature in the NSTML decreases in both 2013 and 2014 when ice thickness in the CCB rebounds from the minimum in 2012. Thus changes in upper ocean heat content between 2008 and 2015 are not attributable to the NSTML but rather are due to temperature increases in the SPWL (40–80 m) (Figure 8f; also see Figures 13b, 13d, and 13f). In fact, the model shows a strong positive temperature trend in the SPWL throughout the whole 1992–2015 period, which is likely due to increasing periods of open water and radiative heating on the Chukchi Shelf and intensifying PW heat transport into the Arctic Ocean through Bering Strait [Woodgate et al., 2012].

6. Concluding Remarks

We have conducted a model-observation synthesis to investigate changes in the upper ocean physics in the CB over the period 1992–2015. The synthesis consists of modeling and assimilation, model validation, and model-observation analysis using MIZMAS, a coupled sea ice-ocean model that assimilates satellite sea ice concentration and SST, and in situ ocean temperature, salinity, and velocity observations. Model bias exists, particularly in overestimating the amplitude of the NSTM. However, MIZMAS replicates the SIZRS observed temperature and salinity profiles in 2013 reasonably well. It also captures the ITP and Seaglider observed temperatures and especially salinities in most depth ranges of the upper ocean in the CB in 2014, with low mean biases and high correlations. In addition, it characterizes the CTD observed depths of isohalines (S 5 31; 33) over the period 2003–2013.

The synthesis results show that the BG has been generally intensifying during 1992–2015, concurrent with a range of changes in sea ice and the upper ocean of the CB. SSH has been generally increasing in conjunction with strengthened anticyclonic ocean circulation and enhanced Ekman convergence and downwelling in the deep basin of the CB and upwelling in the Beaufort Sea shelf break region. Sea ice thickness has been generally decreasing because of accelerated ice melt in late spring and summer, and thinner ice moves faster and has a higher growth rate [Maykut and Untersteiner, 1971] in fall and winter. Salinity has been generally decreasing in the deep basin because of enhanced Ekman convergence and downwelling and ice melt, in addition to increased input of PW [e.g., Woodgate et al., 2012] and Eurasian runoff [Morison et al., 2012], which leads to an increase in isohaline depths and freshwater content. All these changes contribute to a shoaling summer halocline and mixed layer, and a deepening winter halocline and mixed layer in the CB. However, in the Beaufort, Chukchi, and East Siberian shelf and shelf break regions salinity has increased because of enhanced upwelling in the Beaufort shelf break region and the advection of the upwelled saltier water there to the Chukchi and East Siberian shelves. In addition, the increased Ekman convergence draws more water from surrounding areas into the CB, thus reducing SSH in those areas and raising SSH in the CB.

While the BG intensification has been well recognized previously, its possible stabilization in recent years is not as well appreciated. Clues of BG stabilization may be reflected in the reported decrease in liquid freshwater content from 2010 to 2012 [Krishfield et al., 2014; also see Blunden and Arndt, 2014], the weakening of anticyclonic wind and ice circulation during 2011-2013 [Petty et al., 2016], the increase of baroclinic activity in 2013-2014 [Zhao et al., 2016], and the leveling of ocean dynamic height over 2008-2012 [Yoshizawa et al., 2015]. However, we believe that this study is the first attempt to use a model, synthesized with a range of observations, to systematically show the Beaufort Gyre stabilization with greater temporal and spatial coverage and more physical parameters than the previous studies using relatively sparse observations. Our model-observation synthesis results indicate that the BG has been stabilizing over the period 2008-2015, perhaps weakening slightly. This is reflected in the general plateauing since 2008 of SSH, sea ice and ocean speeds, isohaline depths, freshwater content, ice thickness, salinity in various depth ranges (which slightly increases), and halocline and mixed layer depths. The stabilization is also confirmed by the T2014 study that show that the depths of both isohalines (\$ 5 31 and 33) derived using CTD and ITP data over 2003–2013 did not increase from 2008 onward. In fact, they decreased slightly over the period 2008–2013. Another possible sign of stabilization is reflected in the available SIZRS observations that salinity in the upper 15 m increased somewhat from 2012 to 2014 along 1508W in the Beaufort Sea, in contrast to the intensification period when surface waters were generally freshening.

Changes in atmospheric circulation in the CB have a key role in the BG intensification and stabilization. The changes are characterized by generally increasing anticyclonic wind strength and sea level pressure (SLP) before 2008 and falling wind strength and SLP to below-average levels in some years after 2008. Changes in SLP in the CB are highly correlated with changes in ocean surface stress curl and downwelling. Since 2008, Ekman pumping has weakened in much of the CB because of the atmospheric changes, which halts further freshening in the upper ocean, if not slightly reversing it, therefore contributing to the BG stabilization. The general leveling of sea ice thickness in the CB since 2008 also contributes to the stabilization because the simulated ice melt decreases precipitously in 2013 and 2014, limiting a freshwater input to fuel continued intensification.

Whether the BG is intensifying or stabilizing, the simulated SPWL temperature is mostly increasing during 1992–2015. The increase is in response mainly to increased open water and consequently greater radiative heating, and also to enhanced heat transport at Bering Strait [Woodgate et al., 2012]. This also suggests that changes in the CB circulation and stratification have a limited impact on the variability of the SPWL temperature. The changes also have a limited impact on the variability of the NSTML temperature. The simulated NSTML temperature has a relatively small positive trend during 1992–2015, which is closely correlated with decreasing sea ice thickness. It climbs to the highest level in 2012, when Arctic sea ice extent reached a record low, before dropping in 2013–2015 because of the ice thickness rebound.

Note that MIZMAS uses climatological river runoff. Without interannual variability of river freshwater input into the model, the simulated intensification and stabilization are caused solely by changes in sea ice and ocean dynamics and thermodynamics in response to changes in atmospheric circulation. It is less clear what causes the atmospheric changes in the CB. The changes may be linked to large-scale atmospheric dynamics linking the Icelandic and Aleutian low pressure cells and the Beaufort high cell. The atmospheric changes may also be linked to changes in sea ice in the CB, which modifies local air-sea exchange of heat, mass, and momentum. Because of the uncertainties in atmospheric circulation in the future, it remains to be seen whether the BG will continue to maintain the current intensity, or intensify again, or relax, which may have significant climatic and biological consequences.

Acknowledgments

We gratefully acknowledge the support of the Office of Naval Research (grants N00014-12-1-0112, N00014-12-1-0140, N00014-15-1-2295, and N00014-12-1-0180) and the NASA Cryosphere Program (NNX15AG68G). We thank Stephen Okkonen and an anonymous reviewer for their constructive comments. The Ice-Tethered Profiler data were collected and made available by the Ice-Tethered Profiler Program [Toole et al., 2011; Krishfield et al., 2008] based at the Woods Hole Oceanographic Institution (http://www.whoi.edu/itp). Model output is available by contacting zhang@apl.washingon.edu.

References

Aagaard, K., L. Coachman, and E. Carmack (1981), On the halocline of the Arctic Ocean, Deep Sea Res., Part A, 28(6), 529-545. Blunden, J., and D. S. Arndt (2014), State of the climate in 2013, Bull. Am. Meteorol. Soc., 95, S1-S279.

Brugler, E. T., R. S. Pickart, G. W. K. Moore, S. Roberts, T. J. Weingartner, and H. Statscewich (2014), Seasonal to interannual variability of the Pacific Water boundary current in the Beaufort Sea, Prog. Oceanogr., 127, 1–20, doi:10.1016/j.pocean.2014.05.002.

Coachman, L. K., and C. A. Barnes (1961), The contribution of Bering Sea Water to the Arctic Ocean, Arctic, 14, 147-16.

Codispoti, L. A., C. Flagg, V. Kelly, and J. H. Swift (2005), Hydrographic conditions during the 2002 SBI process experiments, Deep-Sea Res., Part II. 52. 3199—3226.

Cole, S. T., F. T. Thwaites, R. A. Krishfield, and J. M. Toole (2015), Processing of velocity observations from Ice-tethered profilers, in MTS/IEEE Oceans 2015 Conference, pp. 1–10, IEEE, Washington D. C.

Gallaher, S. G., T. P. Stanton, W. J. Shaw, S. T. Cole, J. M. Toole, J. P. Wilkinson, T. Maksym, and B. Hwang (2016), Evolution of a Western Arctic ice-ocean boundary layer and mixed layer across a developing thermodynamically forced marginal ice zone, J. Geophys. Res., in press.

Giles, K. A., S. W. Laxon, A. L. Ridout, D. J. Wingham, and S. Bacon (2012), Western Arctic Ocean freshwater storage increased by wind-driven spin-up of the Beaufort Gyre, Nature Geoscience, 5, 194–197.

Gill, A. (1982), Atmosphere-Ocean Dynamics, International Geophysics Series, vol. 30, Academic Press Inc., Cambridge, Mass

Hassol, S. J. (2004), Impacts of a Warming Arctic: Arctic Climate Impact Assessment, 139 pp., Cambridge Univ. Press, N. Y.

Hibler W. D., III, and K. Bryan (1987), A diagnostic ice-ocean model. J. Phys. Oceanogr., 17, 987-1015.

Jackson, J. M., E. C. Carmack, F. A. McLaughlin, S. E. Allen, and R. G. Ingram (2010), Identification, characterization, and change of the near-surface temperature maximum in the Canada Basin, 1993-2008, J. Geophys. Res., 115, C05021, doi:10.1029/2000JC90007.

Kalnay, E., et al. (1996), The NCEP/NCAR 40-year reanalysis project, Bull. Am. Meteorol. Soc., 77, 437-471.

Krishfield, R. A., A. Proshutinsky, K. Tateyama, W. J. Williams, E. C. Carmack, F. A. McLaughlin, and M.-L. Timmermans (2014), Deterioration of perennial seaice in the Beaufort Gyre from 2003 to 2012 and its impact on the oceanic freshwater cycle, J. Geophys. Res. Oceans, 119, 1271–1305, doi:10.1002/2013JC008999.

Krishfield, R., J. Toole, A. Proshutinsky, and M.-L. Timmermans (2008), Automated ice-tethered profilers for seawater observations under pack ice in all seasons, J. Atmos. Ocean. Technol., 25, 2091–2095, doi:10.1175/2008

Kwok, R., G. Spreen, and S. Pang (2013), Arctic sea ice circulation and drift speed: Decadal trends and ocean currents, J. Geophys. Res. Oceans, 118, 2408–2425, doi:10.1002/jgrc.20191.

Large, W. G., J. C. McWilliams, and S. C. Doney (1994), Oceanic vertical mixing: A review and a model with a nonlocal boundary layer parameterization, Rev. Geophys., 32, 363–403.

Lindsay, R., M. Wensnahan, A. Schweiger, and J. Zhang (2014), Evaluation of seven different atmospheric reanalysis products in the Arctic, J. Clim., 27, 2588–2606, doi:10.1175/JCLI-D-13-00014.s1.

Lindsay, R. W., and J. Zhang (2006), Assimilation of ice concentration in an ice-ocean model, J. Atmos. Oceanic. Technol., 23, 742–749.

Manda, A., N. Hirose, and T. Yanagi (2005), Feasible method for the assimilation of satellite-derived SST with an ocean circulation model, J. Atmos. Oceanic Technol., 22(6), 746–756, doi:10.1175/JTECH1744.1.

- Marchuk, G. I., and B. A. Kagan (1989), Dynamics of Ocean Tides, 327 pp., Kluwer Academic Publishers, Dordrecht, the Netherlands.
 Martin, T., M. Steele, and J. Zhang (2014), Seasonality and long-term trend of Arctic Ocean surface stress in a model, J. Geophys. Res. Oceans, 119, 1723–1738. doi:10.1002/2013JC009425.
- Martin, T., M. Tsamados, D. Schroeder, and D. L. Feltham (2016), The impact of variable sea ice roughness on changes in Arctic Ocean surface stress: A model study, J. Geophys. Res. Oceans, 121, 1931–1952, doi:10.1002/2015
- Mauritzen, C., B. Rudels, and J. Toole (2013), Chapter 17: The Arctic and Subarctic Oceans/Seas., Ocean Circulation and Climate, 2nd ed., edited by J. Church et al., pp. 443–464, Academic.
- Maykut, G. A., and N. Untersteiner (1971), Some results from a time-dependent thermo-dynamic model of sea ice, J. Geophys. Res., 76, 1550–1575.
- McLaughlin, F. A., and E. C. Carmack (2010), Deepening of the nutricline and chlorophyll maximum in the Canada Basin interior, 2003–2009, Geophys. Res. Lett., 37, L24602, doi:10.1029/2010GL045459.
- McLaughlin, F. A., E. C. Carmack, W. J. Williams, S. Zimmermann, K. Shimada, and M. Itoh (2009), Joint effects of boundary currents and thermohaline intrusions on the warming of Atlantic water in the Canada Basin, 1993–2007, J. Geophys. Res., 114, C00A12, doi:10.1029/2008JC005001.
- McPhee, M. G. (2013), Intensification of geostrophic currents in the Canada Basin, Arctic Ocean, J. Clim., 26(10), 3130-313.
- Morison, J., R. Kwok, C. Peralta-Ferriz, M. Alkier, I. Rigor, R. Anderson, and M. Steele (2012), Changing Arctic Ocean freshwater pathways, Nature. 481. 66–70. doi:10.1038/nature10705.
- Overland, J. E., J. M. Adams, and N. A. Bond (1999), Decadal variability of the Aleutian low and its relation to high-latitude circulation, J. Clim., 12, 1542–1548.
- Parkinson, C. L., and J. C. Comiso (2013), On the 2012 record low Arctic sea ice cover: Combined impact of preconditioning and an August storm, Geophys. Res. Lett., 40, 1356–1361, doi:10.1002/grl.50349.
- Peralta-Ferriz, C., and R. A. Woodgate (2015), Seasonal and interannual variability of pan-Arctic surface mixed layer properties from 1979 to 2012 from hydrographic data, and the dominance of stratification for multiyear mixed layer depth shoaling, Prog. Oceanogr. 134, 19–53.
- Perovich, D. K., B. Light, H. Eicken, K. F. Jones, K. Runciman, and S. V. Nghiem (2007), Increasing solar heating of the Arctic Ocean and adjacent seas, 1979–2005: Attribution and role in the ice-albedo feedback, Geophys. Res. Lett., 34, L19505, doi:10.1029/2007GL031480.
- Perovich, D. K., J. A. Richter-Menge, and K. F. Jones (2008), Sunlight, water, and ice: Extreme Arctic sea ice melt during the summer of 2007, Geophys. Res. Lett., 35, L11501, doi:10.1029/2008GL034007.
- Petty, A. A., J. K. Hutchings, J. A. Richter-Menge, and M. A. Tschudi (2016), Sea ice circulation around the Beaufort Gyre: The changing role of wind forcing and the sea ice state, J. Geophys. Res. Oceans., 121, 3278–3296, doi:10.1002/2015JC010903.
- Pisareva, M. N., R. S. Pickart, M. A. Spall, C. Nobre, D. J. Torres, G. W. K. Moore, and T. E. Whitledge (2015), Flow of Pacific water in the western Chukchi Sea: Results from the 2009 RUSALCA expedition, Deep Sea Res., Part II, 105, 53–73, doi:10.1016/j.dsr.2015.08.
- Proshutinsky, A., R. Krishfield, M.-L. Timmermans, J. Toole, E. Carmack, F. McLaughlin, W. J. Williams, S. Zimmermann, M. Itoh, and K. Shimada (2009), Beaufort Gyre freshwater reservoir: State and variability from observations. J. Geophys. Res., 114, C00A10, doi: 10.1029/2008JC005104.
- Rabe, B., M. Karcher, U. Schauer, J. M. Toole, R.A. Krishfield, S. Pisarev, F. Kauker, R. Gerdes, and T. Kikuchi (2011), An assessment of Arctic Ocean freshwater content changes from the 1990s to the 2006 2008 period, Deep Sea Res., Part I, 58, 173–185, doi:10.1016/i.dsr.2010.12.002.
- Rampal, P., J. Weiss, and D. Marsan (2009), Positive trend in the mean speed and deformation rate of Arctic sea ice, 1979–2007, J. Geophys. Res., 114, C05013, doi:10.1029/2008JC005066.
- Schweiger, A., and J. Zhang (2015), Accuracy of short-term sea ice drift forecasts using a coupled ice-ocean model, J. Geophys. Res. Oceans, 120, 7827–7841, doi:10.1002/2015JC011273.
- Schweiger, A., R. W. Lindsay, J. Zhang, M. Steele, H. Stern, and R. Kwok (2011), Uncertainty in modeled Arctic sea ice volume, J. Geophys. Res., 116, C00D06, doi:10.1029/2011JC007084.
- Serreze, M. C., M. M. Holland, and J. Stroeve (2007), Perspectives on the Arctic's shrinking sea-ice cover, Science, 315, 1533-1536.
- Shimada K., T. Kamoshida, M. Itoh, S. Nishino, E. Carmack, F. A. McLaughlin, S. Zimmermann, and A. Proshutinsky (2006), Pacific Ocean inflow: Influence on catastrophic reduction of sea ice cover in the Arctic Ocean, Geophys. Res. Lett., 33, L08605, doi:10.1029/ 2005GL025624.
- Smith, R. D., J. K. Dukowicz, and R. C. Malone (1992), Parallel Ocean General Circulation Modeling, Physica D, 60, 38–61.
- Steele, M., J. Morison, W. Ermold, I. Rigor, M. Ortmeyer and K. Shimada (2004), Circulation of summer Pacific halocline water in the Arctic Ocean, J. Geophys. Res., 109, C02027, doi:10.1029/2003JC002009.
- Steele, M., W. Ermold, and J. Zhang (2008), Arctic Ocean surface warming trends over the past 100 years, Geophys. Res. Lett., 35, L02614, doi:10.1029/2007GL031651.
- Steele, M., J. Zhang, and W. Ermold (2010), Mechanisms of summertime upper Arctic Ocean warming and the effect on sea ice melt, J. Geophys. Res., 115, C11004, doi:10.1029/2009JC005849.
- Steele, M., W. Ermold, and J. Zhang (2011), Modeling the formation and fate of the near-surface temperature maximum in the Canadian Basin of the Arctic Ocean, J. Geophys. Res., 116, C11015, doi:10.1029/2010JC006803.
- Timmermans, M-L., A. Proshutinsky, E. Golubeva, J. M. Jackson, R. Krishfield, M. McCall, and G. Platov (2014), Mechanisms of Pacific Summer Water variability in the Arctic's Central Canada Basin, J. Geophys. Res. Oceans, 119, 7523–7548, doi:10.1002/2014JC010273.
- Toole, J. M., R. A. Krishfield, M.-L. Timmermans and A. Proshutinsky (2011), The ice-tethered profiler: Argo of the Arctic, Oceanography, 24(3), 126–135, doi:10.5670/oceanog.2011.64.
- Toole, J. M., M.-L. Timmermans, D. K. Perovich, R. A. Krishfield, A. Proshutinsky, and J. A. Richter-Menge (2010), Influences of the Ocean Surface mixed layer and thermohaline stratification on Arctic Sea Ice in the Central Canada Basin, J. Geophys. Res., 115, C10018, doi: 10.1029/2009JC005660.
- Walsh, J. E., W. L. Chapman, and T. L. Shy (1996), Recent decrease of sea level pressure in the central Arctic, J. Clim., 9, 480–486. Weingartner, T., K. Aagaard, R. Woodgate, S. Danielson, Y. Sasaki, and D. Cavalieri (2005), Circulation on the north central Chukchi Sea shelf,
- Deep-Sea Res. Part II, 52, 3150–3174.
 Woodgate, R. A., K. Aagaard and T. J. Weingartner (2005), Monthly temperature, salinity, and transport variability of the Bering Strait through flow, Geophys. Res. Lett., 32, L04601, doi:10.1029/2004GL021880.
- Woodgate, R. A., T. Weingartner, and R. Lindsay (2010), The 2007 Bering Strait oceanic heat flux and anomalous Arctic sea-ice retreat, Geophys. Res. Lett., 37, L01602, doi:10.1029/2009GL041621.
- Woodgate, R. A., T. J. Weingartner, and R. Lindsay (2012), Observed increases in Bering Strait oceanic fluxes from the Pacific to the Arctic from 2001 to 2011 and their impacts on the Arctic Ocean water column, Geophys. Res. Lett., 39, L24603, doi:10.1029/2012GL054092.

- Yamamoto-Kawai, M., F. A. McLaughlin, E. C. Carmack, S. Nishino, K. Shimada, and N. Kurita (2009), Surface freshen-ing of the Canada Basin, 2003–2007: river runoff versus sea ice meltwater, J. Geophys. Res., 114, C00A05.
- Yang J. (2009), Seasonal and interannual variability of downwelling in the Beaufort Sea, J. Geophys. Res., 114, C00A14, doi:10.1029/ 2008.JC005084.
- Yoshizawa, E., K. Shimada, H. K. Ha, T. W. Kim, S. H. Kang, and K. H. Chung (2015), Delayed responses of the oceanic Beaufort Gyre to winds and sea ice motions: Influences on variations of sea ice cover in the Pacific sector of the Arctic Ocean, J. Oceanogr., 71, 187–197, doi: 10.1007/s10872-015-0276-6.
- Zhang, J. (2005), Warming of the arctic ice-ocean system is faster than the global average since the 1960s, Geophys. Res. Lett., 32, L19602, doi:10.1029/2005GL024216.
- Zhang, J., and D. A. Rothrock (2003), Modeling global sea ice with a thickness and enthalpy distribution model in generalized curvilinear coordinates, Mon. Weather Rev., 131(5), 681–697.
- Zhang, J., and M. Steele (2007), The effect of vertical mixing on the Atlantic water layer circulation in the Arctic Ocean, J. Geophys. Res., 112, C04S04, doi:10.1029/2006.IC003732
- Zhang, J., W. D. Hibler, M. Steele, and D. A. Rothrock (1998), Arctic ice-ocean modeling with and without climate restoring, J. Phys. Oceanogr., 28, 191–217.
- Zhang, J., M. Steele, and R. Woodgate (2008), The role of Pacific water in the dramatic retreat of arctic sea ice during summer 2007, J. Polar Sci., 19(2), 93–107.
- Zhang, J., R. Woodgate, and R. Moritz (2010), Sea ice response to atmospheric and oceanic forcing in the Bering Sea, J. Phys. Oceanogr., 40, 1729–1747, doi:10.1175/2010JPO4323.1.
- Zhang, J., R. Lindsay, A. Schweiger, and I. Rigor (2012), Recent changes in the dynamic properties of declining Arctic sea ice: A model study, Geophys. Res. Lett., 39, L20503, doi:10.1029/2012GL053545.
- Zhang, J., R. Lindsay, A. Schweiger, and M. Steele (2013), The impact of an intense summer cyclone on 2012 Arctic sea ice retreat, Geophys. Res. Lett., 40, 720–726, doi:10.1002/grl.50190.
- Zhang, J., C. Ashjian, R. Campbell, Y.H. Spitz, M. Steele, and V. Hill (2015), The influence of sea ice and snow cover and nutrient availability on the formation of massive under-ice phytoplankton blooms in the Chukchi Sea, Deep Sea Res. Part II, 118, 122–135, doi:10.1016/j.dsr2.2015.02.008.
- Zhao, M., M.-L. Timmermans, S. Cole, R. Krishfield, and J. Toole (2016), Evolution of the eddy field in the Arctic Ocean's Canada Basin, 2005–2015, Geophys. Res. Lett., 43, 8106–8114, doi:10.1002/2016GL069671.